ACS Catalysis

Research Article

pubs.acs.org/acscatalysis

Shape Effect of ZnO Crystals as Cocatalyst in Combined Reforming–Hydrogenolysis of Glycerol

Jiye Hu,[†] Yiqiu Fan,[†] Yan Pei,[†] Minghua Qiao,*[,†] Kangnian Fan,[†] Xiaoxin Zhang,[‡] and Baoning Zong*[,‡]

[†]Department of Chemistry and Shanghai Key Laboratory of Molecular Catalysis and Innovative Materials, Fudan University, Shanghai 200433, People's Republic of China

[‡]State Key Laboratory of Catalytic Materials and Reaction Engineering, Research Institute of Petroleum Processing, Beijing 100083, People's Republic of China

ABSTRACT: Disk- and rod-shaped hexagonal ZnO crystals with various length-to-diameter aspect ratios were controllably synthesized via a facile solution route by adjusting the precursor concentration. The shape and the dimension of the synthesized ZnO crystals were observed by scanning electron microscopy (SEM). The wurtzite structure and the growth habit were determined by powder X-ray diffraction (XRD) and transmission electron microscopy (TEM) coupled with selected-area electron diffraction (SAED). It is found that with the lowering of the precursor concentrations, the ZnO crystals were elongated along the *c*-axis, and the diameter of the {001} planes was reduced, leading to shape evolution from hexagonal disk to prismatic rod. As a result, the ZnO crystals were different from each other in the proportion of the {100} nonpolar planes and the {001} polar planes. The well-defined ZnO crystals were used as the cocatalyst with skeletal $Ni_{40}Mo_{10}$ in the combined reforming–hydrogenolysis (CRH) of glycerol in the absence of adventitious H_2. A remarkable shape-dependent effect on the selectivity to the C3 hydrogenolysis products and the production rate of 1,2-propandiol (1,2-PDO) was identified. ZnO with a larger proportion of the nonpolar planes was more effective in the CRH of glycerol to the C3 products. An excellent linear relationship between the surface area of the {100} nonpolar planes and the production rate of 1,2-PDO was identified. This is attributed to the in situ enhancement of the Lewis acidity of the nonpolar planes of ZnO by chemisorbed CO_2 from the reforming of glycerol, which greatly accelerates the dehydration of glycerol to acetol, the intermediate to 1,2-PDO.

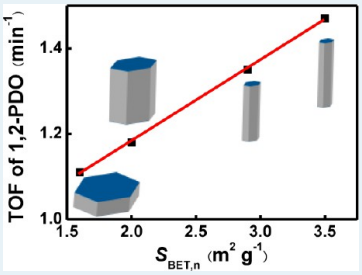

KEYWORDS: *shape, zinc oxide, glycerol, hydrogenolysis, promotion effect*

1. INTRODUCTION

Glycerol, as the main byproduct of biodiesel derived from biomass, is currently widely available.[1,2] Because it is highly functionalized, glycerol is considered a versatile platform chemical for the production of a set of valuable chemicals.[3] Among various utilization routes of glycerol, its reaction with H_2 to produce 1,2-PDO is of special interest[4−8] because 1,2-PDO is a desirable chemical that has wide applications in the cosmetic, pharmaceutical, and polymer industries.[1,2,9] Traditionally, 1,2-PDO is fabricated in the petrochemical route through the hydration of hazardous propylene oxide.[1] Production of 1,2-PDO from biomass-derived glycerol is obviously more sustainable and environmentally more friendly.

In the hydrogenolysis of glycerol to 1,2-PDO, H_2 can be fed into the reactor externally or generated on-site by converting a portion of glycerol over catalysts with reforming ability.[10] The concept of on-site H_2 generation can produce 1,2-PDO from glycerol with high atomic economy and operational safety, thus attracting much attention. Many works have been focused on the conversion of glycerol to 1,2-PDO without adventitious H_2. D'Hondt et al. achieved the production of 1,2-PDO from glycerol under an inert atmosphere over the noble Pt/NaY catalyst.[11] This leading work triggered successive research in pursuing other effective catalyst systems. Roy et al. reported that an admixture catalyst comprising equal weights of Ru/Al_2O_3 and Pt/Al_2O_3 showed a synergetic effect between them, leading to glycerol conversion of 50.1% with 1,2-PDO selectivity of 47.2% at 493 K under 1.4 MPa N_2 for 6 h.[12] They found that, as compared with N_2 atmosphere, H_2 atmosphere adversely affected 1,2-PDO selectivity on their catalyst because of excessive methanation. Gandarias et al. reported that the amorphous silicoalumina-supported Pt catalyst (Pt/ASA) gave glycerol conversion of 26.6% with 1,2-PDO selectivity of 35.3% at 493 K under 4.5 MPa N_2 for 24 h.[13] Wawrzetz et al. investigated the glycerol transformation over the Pt/Al_2O_3 catalyst under N_2 atmosphere in a continuous fixed-bed reactor.[14] By kinetically controlled experiments, they disclosed that 1,2-PDO was formed through glycerol dehydration to acetol on the support, followed by acetol hydrogenation on the metal.

Recently, we found that when physically mixed with the rapidly quenched skeletal NiMo catalyst (RQ $Ni_{40}Mo_{10}$), ZnO was far superior to other oxides in directing the product to 1,2-PDO in the CRH of glycerol.[15] In light of the study by Wang et al. on CO_2 adsorption on (100) nonpolar plane of ZnO,[16,17] we tentatively attributed the promotion effect to CO_2-enhanced

Received: July 8, 2013
Revised: August 28, 2013
Published: August 29, 2013

   dx.doi.org/10.1021/cs400526s | ACS Catal. 2013, 3, 2280−2287

Lewis acidity of ZnO, which accelerates the dehydration of glycerol to acetol, the reaction intermediate to 1,2-PDO. However, the commercial ZnO has ill-defined morphology, which makes it difficult to quantify the effect of the nonpolar plane of ZnO on the promotion effect. Such knowledge may offer new opportunity for maximizing the beneficial effect of ZnO in the CRH of glycerol through rational shape control.

Regular crystal with well-defined morphology and limited surface sites is conductive to a better understanding of the microscopic origin of its function in heterogeneous catalysis.[18] It is documented that ZnO crystal tends to take on a prismatic shape with two hexagonal {001} bottom planes and six {100} side planes.[19] The two {001} planes are terminated with either Zn^{2+} or O^{2-} ions and are, thus, polar, whereas the six {100} planes are terminated with both ions and are, thus, nonpolar.[20] The solution route is versatile in synthesizing ZnO crystals with adjustable growth habits.[21,22] With these shape-controlled ZnO crystals, one may find a direct correlation between the surface area of the nonpolar planes and the promotion effect of ZnO in the CRH of glycerol, provided that our previous argument based on commercial ZnO is justified.

In the present work, we synthesized hexagonal ZnO crystals with different exposure degrees of the nonpolar planes by the solution method and physically mixed them with RQ $Ni_{40}Mo_{10}$ for the CRH of glycerol. The physical properties of the ZnO crystals were characterized by XRD, SEM, and TEM coupled with SAED, Raman spectroscopy, photoluminescence (PL) spectroscopy, and N_2 physisorption. The possible electronic interaction between ZnO and RQ $Ni_{40}Mo_{10}$ was discriminated by X-ray photoelectron spectroscopy (XPS). Correlations of the structural peculiarities of the ZnO crystals with their promotion effects in the CRH of glycerol were discussed on the basis of detailed catalytic results.

2. EXPERIMENTAL SECTION

2.1. Preparation of ZnO. The preparation procedure for hexagonal ZnO crystals with disk to rod shapes was a modification of the method developed by Li et al.[21] with some adjustments in the precursor concentration and the crystallization temperature and time. First, 3.00 g of $Zn(CH_3COO)_2{\cdot}2H_2O$ ($ZnAc_2$) and 1.92 g of hexamethylenetetramine (HMT) were dissolved in 24, 120, 240, and 360 mL of deionized water. After ultrasonication for 10 min, transparent solutions with decreasing precursor concentrations were obtained. These vessels were covered by preservative films and kept at 363 K for 12 h. After being cooled to room temperature, the white precipitates were collected by centrifugation and washed with ethanol, followed by deionized water to neutrality. The products were dried at 333 K overnight and calcined at 473 K for 2 h in air for the purpose of characterization and catalytic testing.

2.2. Characterization. The XRD patterns were acquired on a Bruker AXS D8 Advance X-ray diffractometer using Ni-filtered Cu Kα radiation (λ = 0.15418 nm). The tube voltage was 40 kV, and the current was 40 mA.

The SEM images were recorded on a Philips XL30 electron microscope. The accelerating voltage was 20−30 kV. The samples were attached to a double-sided carbon conductive tape on an aluminum slab and coated with gold. TEM observations were conducted on a JEOL JEM2011 microscope operated at 200 kV. The ZnO samples were dispersed in ethanol, dropped onto a carbon-film-coated copper grid, and dried in air.

The Raman spectra were recorded on a Jobin-Yvon LabRam-1B spectrometer with spectral resolution of ~1.2 cm^{-1}. The laser line at 632 nm of a He−Ne laser with an output of 4.3 mW was used as the excitation source.

Room temperature PL spectra were acquired on an Edinburgh Photonics FLS 920 photoluminescence instrument with an excitation wavelength of 325 nm. Prior to the measurements, the ZnO samples were dispersed in deionized water by ultrasonication to prepare homogeneous suspension with the same concentration of 1.0 mg mL^{-1}.

The XPS spectra were recorded on a Perkin-Elmer PHI5000C spectrometer using Mg Kα radiation ($h\nu$ = 1253.6 eV) as the excitation source. The samples were pressed into a self-supported disc and loaded onto the sample plate, then the samples were degassed in the pretreatment chamber in vacuo at room temperature for 4 h before being transferred to the analyzing chamber with a background pressure >2 × 10^{-9} Torr. All binding energy (BE) values were referenced to the C 1s peak of contaminant carbon at 284.6 eV with an uncertainty of ±0.2 eV.

The multipoint Brunauer−Emmett−Teller (BET) surface areas of the ZnO samples were measured by N_2 physisorption at 77 K on a Micromeritics TriStar3000 apparatus. Prior to the measurements, the samples were purged by N_2 at 423 K for 2 h.

2.3. Activity Testing and Product Analysis. The CRH of glycerol was conducted on a continuous-flow fixed-bed tubular reactor (6 mm i.d.). The reaction temperature was 508 K, and the system pressure was 3.1 MPa regulated by Ar. An aqueous solution containing 10 wt % of glycerol was pumped from the bottom of the reactor at varying flow rates to obtain the desired weight hourly space velocity (WHSV, weight of glycerol per weight of RQ $Ni_{40}Mo_{10}$ per hour). The weight ratio between ZnO and RQ $Ni_{40}Mo_{10}$ in the physically mixed ZnO−RQ $Ni_{40}Mo_{10}$ catalysts was kept at 1:1. The reaction course was monitored by sampling the gas and liquid products at intervals, followed by gas chromatographic analysis. In the gas products, H_2 and CO_2 were separated by a 5 Å molecular sieve-packed column and examined by a thermal conductivity detector (TCD) on a GC102 M gas chromatograph. Light alkanes were separated by a Porapak R packed column and examined by a flame ionization detector (FID) on the same gas chromatograph. The liquid products were condensed and separated by a CP-Wax 52 CB capillary column (30 m × 0.25 mm × 0.25 μm) and examined by an FID on a GC9560 gas chromatograph. The liquid products were also qualified by GC/MS (Finnigan Voyager) with an HP-5 capillary column. The carbon balance was within ±5% for all catalytic runs.

3. RESULTS

3.1. Crystal Phase and Morphology. The crystal phase and phase purity of the ZnO samples were examined by XRD. As presented in Figure 1, all the diffraction peaks can be indexed to ZnO with hexagonal wurtzite structure (space group $P6_3mc$, JCPDS 36-1451).[23] The intense and sharp diffraction peaks indicate that these ZnO crystals are in general of high crystallinity. No impurity peaks were found. It is noted that the relative intensities between the (100) and (002) diffraction peaks are quite different among these samples. As implemented in the brackets in Figure 1, the $I_{(100)}/I_{(002)}$ intensity ratio increases in the order of 0.80 < 1.05 < 1.77 < 2.61 with the decrease in the precursor concentration, indicating the preferential growth of the ZnO crystals along the *c*-axis.[21]

dx.doi.org/10.1021/cs400526s | ACS Catal. 2013, 3, 2280−2287

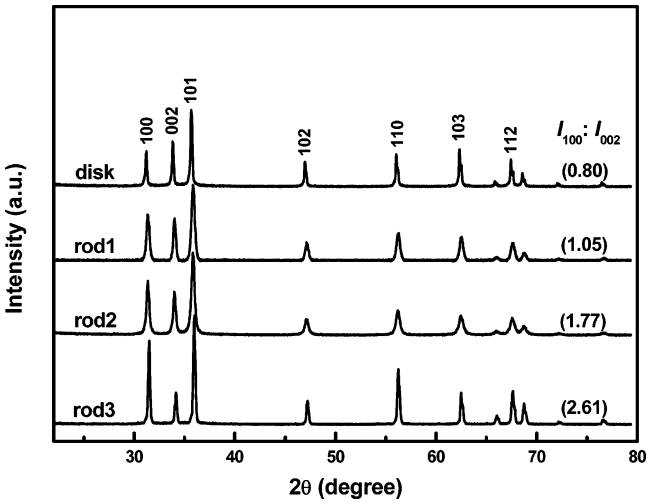

Figure 1. XRD patterns of the ZnO-disk, ZnO-rod1, ZnO-rod2, ZnO-rod3 samples.

SEM unambiguously confirmed the shape change of ZnO from disk to rod with the lowering of the precursor concentration. According to Figure 2a, relatively uniform and perfect hexagonal ZnO disks were harvested from the highest precursor concentration. By reducing the precursor concentration, the diameter of the hexagonal surface was reduced and the length was increased, giving rise to hexagonal ZnO prismatic rods with six smooth planes throughout their length (Figure 2b, c, d). This concentration-dependent shape change is in accordance with the observation by Vayssieres.[24] On the basis of the shape, we labeled these ZnO crystals as ZnO-disk (Figure 2a), ZnO-rod1 (Figure 2b), ZnO-rod2 (Figure 2c), and ZnO-rod3 (Figure 2d). As summarized in Table 1, from ZnO-disk to ZnO-rod3, the average length increased monotonically from 1.4 to 5.7 μm, and the average diameter of the hexagonal plane decreased monotonically from 5.6 to 1.3 μm, resulting in a drastic increase in the length-to-diameter aspect ratio from 0.3 to 4.4.

Table 1. Physical Characteristics of the As-Synthesized ZnO Samples

sample	length (μm)	diameter (μm)	R^a	$S_{BET}{}^b$ ($m^2\ g^{-1}$)	$S_{BET,n}{}^c$ ($m^2\ g^{-1}$)
ZnO-disk	1.4 ± 0.2	5.6 ± 1.4	0.3	4.7	1.6
ZnO-rod1	4.7 ± 1.5	4.0 ± 1.4	1.2	2.9	2.0
ZnO-rod2	4.9 ± 1.7	1.5 ± 0.6	3.3	3.4	2.9
ZnO-rod3	5.7 ± 1.8	1.3 ± 0.4	4.4	3.9	3.5

[a]Length-to-diameter aspect ratio. [b]Total specific surface area determined by N_2 physisorption. [c]Specific surface area of the nonpolar surfaces calculated from the total specific surface area and the dimension of the ZnO measured by SEM.

The microstructures of the ZnO crystals were elucidated by TEM using ZnO-disk and ZnO-rod3 as examples for the disk- and rod-shaped ZnO samples, respectively. Figure 3a is the plan view of ZnO-disk, which clearly evidenced the regular hexagonal shape fully consistent with the SEM observation. The SAED pattern of ZnO-disk as the inset in Figure 3a can be

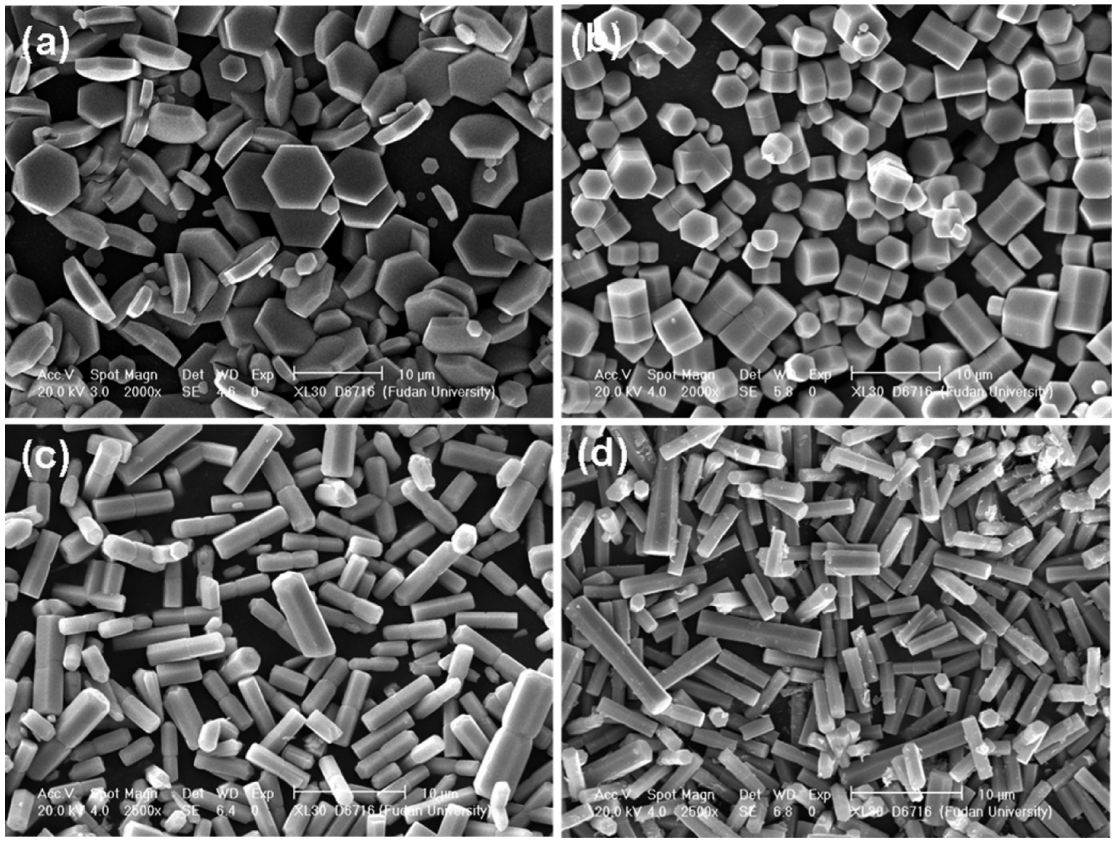

Figure 2. SEM images of (a) ZnO-disk, (b) ZnO-rod1, (c) ZnO-rod2, and (d) ZnO-rod3.

dx.doi.org/10.1021/cs400526s | ACS Catal. 2013, 3, 2280−2287

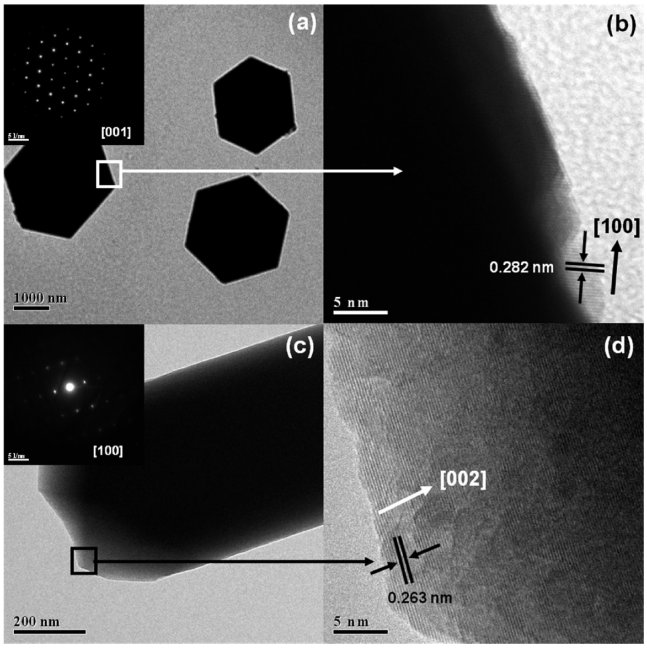

Figure 3. (a) TEM image and (b) HRTEM image of ZnO-disk. Inset in part a shows the corresponding SAED pattern. (c) TEM image and (d) HRTEM image of ZnO-rod3. Inset in part c shows the corresponding SAED pattern.

indexed to the diffraction along the [001] zone axis,[25,26] which reflects the single-crystalline nature of the ZnO disk with hexagonal {001} polar surfaces. The high-resolution TEM (HRTEM) image of this sample is presented in Figure 3b. The ordered lattice fringes with the interplanar spacing of 0.282 nm is clearly seen at the crystal edge, which can be ascribed to the {100} nonpolar planes of wurtzite ZnO.[27,28] Figure 3c presents the side view of ZnO-rod3. The corresponding SAED pattern is indexed as the [100] zone spots,[29] which also evidence the high crystal quality of the ZnO rods. The HRTEM image of ZnO-rod3 (Figure 3d) shows ordered lattice fringes with the interplanar spacing of ~0.263 nm, which coincides with the {002} planes of wurtzite ZnO[30,31] and confirms the [001] orientation of the ZnO rods.

It is acknowledged that many factors integrate to affect the nucleation and growth of a crystal, thus leading to different shapes.[32] In the present synthesis process, the precursors and preparation conditions (temperature and time) were identical. The only difference was the precursor concentration used. Therefore, the precursor concentration must be largely responsible for the shape difference of the ZnO crystals. In the preparation, $ZnAc_2$ is the zinc source and also supplies Ac^- ions, and HMT serves as the pH buffer and provides a slow and continuous supply of OH^- ions.[32,33] According to Peng et al.,[22] at higher precursor concentration, the Ac^- ions are more inclined to adsorb on the (001) polar plane of ZnO terminated with Zn cations, which inhibits the growth along the *c*-axis and, consequently, giving rise to ZnO disks, although at lower precursor concentration, the OH^- ions that functions as the precipitant[34] tend to substitute Ac^- and adsorb on the (001) polar plane.[21] The adsorption of the OH^- ions will accelerate the growth of the (001) plane, resulting in the formation of ZnO rods elongated at the *c*-axis. The above argument justifies the observed decrease in the diameter and increase in the length of the hexagonal ZnO crystals with the lowering of the precursor concentration.

3.2. Optical Properties. Figure 4 shows the Raman spectra of the ZnO crystals. There is a prominent feature peaked at

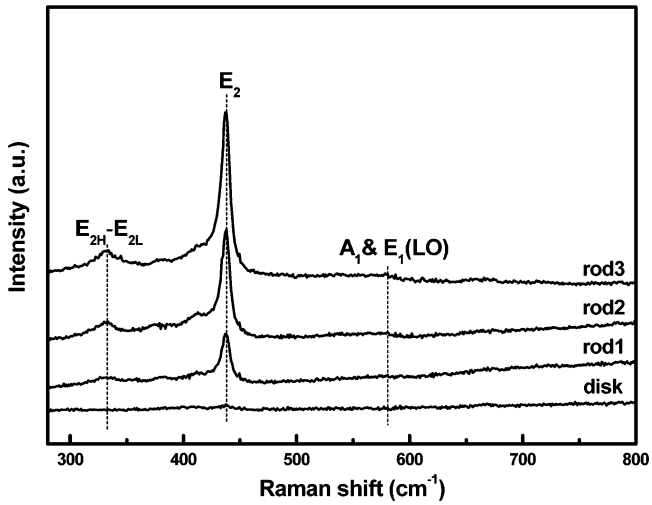

Figure 4. Raman spectra of the ZnO-disk, ZnO-rod1, ZnO-rod2, and ZnO-rod3 samples.

~437 cm^{-1} in all spectra, which is characteristic of the Raman active optical-phonon E_2 mode of hexagonal wurtzite ZnO.[35] Some weak features at around 333 cm^{-1} were also observed, which are assigned to the multiphonon $E_{2H}-E_{2L}$ modes.[28,35] The virtual absence of the scattering peaks at 550–600 cm^{-1} due to a superimposition of the A_1 and E_1 (LO) modes evidences the good phase purity of the ZnO crystals.[28,36] It is also observed that the E_2 mode became stronger with the increase in the aspect ratio, implying that the crystallinity of ZnO became better from ZnO-disk to ZnO-rod3.[37]

Room-temperature PL spectra of the ZnO samples are shown in Figure 5. In all cases, the luminescence band at around 385 nm and the broad band centered at 609 nm are observed. The former resulted from the near-band edge emission of the wide band gap ZnO,[38] and the latter in the

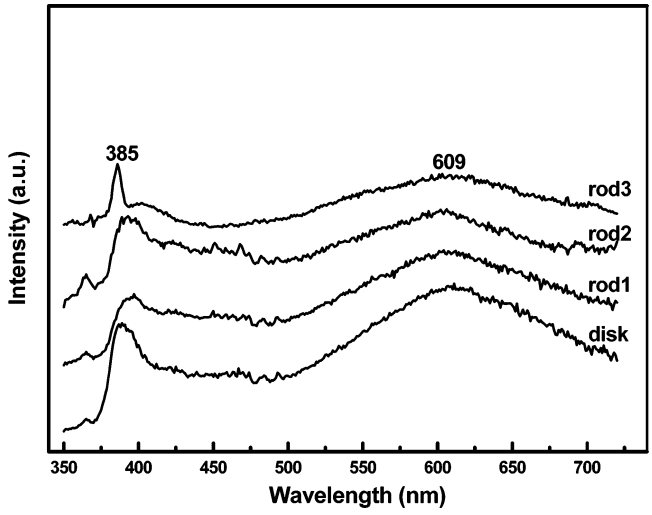

Figure 5. Room-temperature PL spectra of the ZnO-disk, ZnO-rod1, ZnO-rod2, and ZnO-rod3 samples.

dx.doi.org/10.1021/cs400526s | ACS Catal. 2013, 3, 2280–2287

visible-light region is assigned as an overall reflection of surface detects,[21,39] such as oxygen vacancy and interstitial defects.[40,41] Judging from the intensities of the visible-light region bands, we found that the peak intensity follows the order of ZnO-disk > ZnO-rod1 > ZnO-rod2 > ZnO-rod3, which is consistent with the observation by Li et al. when comparing the PL spectra of their ZnO disk with the rod.[21] It indicates that the amount of the surface defects on these ZnO samples decreased in that order. As claimed by Strunk et al.,[42] the {100} nonpolar planes, which is more abundant on the ZnO sample with the higher aspect ratio, have low surface energies and, thus, are more stable than the high-energy {001} polar planes, so to minimize the total surface energy, the dissolution of the high-energy polar planes, although invisible by SEM or TEM, is faster than that of the nonpolar planes, which introduces more surface defects on the ZnO sample abundant in the {001} polar planes.[21]

3.3. Catalytic Results in the CRH of Glycerol. The synthesis of the ZnO crystals exposing different proportions of the polar and nonpolar planes allows us to differentiate their respective influence in the CRH of glycerol. The detailed physicochemical properties of RQ $Ni_{40}Mo_{10}$ have been described elsewhere.[15] The ZnO−RQ $Ni_{40}Mo_{10}$ catalysts were homogeneous mixtures of ZnO with different crystal shapes and RQ $Ni_{40}Mo_{10}$ with a weight ratio of 1:1. Previous work using commercial ZnO as the cocatalyst has shown that this weight ratio could present a good promotion effect.[15]

Table 2 compiles the catalytic results over bare RQ $Ni_{40}Mo_{10}$ and the ZnO−RQ $Ni_{40}Mo_{10}$ admixture catalysts at high conversion levels of glycerol. Aqueous-phase transformation of glycerol over heterogeneous catalysts involves complicated reaction networks;[43,44] however, this process can be approximately categorized into two kinds of pathways in parallel: namely, reforming and hydrogenolysis, involving C−C bond cleavage and C−O bond cleavage, respectively.[45] Thus, to ease the interpretation of the catalytic results, we classified the products into three groups in Table 2: (i) gas products resulting from the aqueous-phase reforming (APR) of glycerol and successive gas phase reactions, (ii) hydrogenolysis products resulting from the dehydration/hydrogenation reactions, and (iii) cracking products in the liquid phase resulting from C−C bond cleavage of glycerol or C_3 intermediates. According to Table 2, the product distributions over these catalysts were qualitatively similar to that over the Pt/Al_2O_3 catalyst.[14] Bare RQ $Ni_{40}Mo_{10}$ gave 42% selectivity to the hydrogenolysis products, with 32% selectivity to 1,2-PDO. In the presence of ZnO, all four ZnO−RQ $Ni_{40}Mo_{10}$ admixture catalysts exhibited improved selectivities to the hydrogenolysis products inclusive of 1,2-PDO. It is particularly noteworthy that from ZnO-disk to ZnO-rod3, the selectivity to the hydrogenolysis products improved from 51% to 72% with the concomitant improvement of the selectivity to 1,2-PDO from 38% to 51%. Meanwhile, the selectivities to the gas and cracking products dropped from 31% to 17% and from 18% to 11%, respectively. Interestingly, the order of the selectivity to the hydrogenolysis products as well as 1,2-PDO is consistent with the order of the aspect ratio of the ZnO crystals, which infers an inherent connection between the product distributions and the shapes of the ZnO crystals in the CRH of glycerol.

Table 2. Catalytic Results of the ZnO−RQ $Ni_{40}Mo_{10}$ Admixture Catalysts in the CRH of Glycerol with ZnO Crystals of Different Shapes[a]

		carbon-based product selectivity (%)		
ZnO	conversion (%)	gas[b]	hydrogenolysis[c]	cracking[d]
none	99	41	42 (32)	17
disk	98	31	51 (38)	18
rod1	99	27	56 (41)	16
rod2	97	21	67 (49)	13
rod3	98	17	72 (51)	11

[a]Reaction conditions: T = 508 K, p_{Ar} = 3.1 MPa, ZnO/RQ $Ni_{40}Mo_{10}$ weight ratio = 1.0, WHSV = 1.2 h^{-1} (relative to RQ $Ni_{40}Mo_{10}$), and t = 8 h. [b]Gas products (including CO_2 and light alkanes). [c]Hydrogenolysis products (including acetone, 1-propanol, 2-propanol, acetol, propionic acid, and 1,2-PDO). In the parentheses is the selectivity to 1,2-PDO. [d]Cracking products in liquid phase (including methanol, ethanol, acetaldehyde, acetic acid, and ethylene glycol).

In an endeavor to relate the production rate of 1,2-PDO to the shapes of the ZnO crystals, kinetically controlled experiments were carried out by adjusting the WHSV to restrict the glycerol conversion within the range of 10%−15% to exclude the transport limitations.[46] Figure 6 presents the production rate of 1,2-PDO expressed as turnover frequency (TOF) with respect to the metallic Ni sites. In compliance with our previous work using commercial ZnO as the cocatalyst,[15] the figure clearly illustrates that the physically mixed ZnO markedly improved the TOF of 1,2-PDO. The TOF of 1,2-PDO was 0.72 min^{-1} on bare RQ $Ni_{40}Mo_{10}$ and markedly increased to 1.1 min^{-1} on the ZnO-disk−RQ $Ni_{40}Mo_{10}$ catalyst. The TOF of 1,2-PDO was increased steadily with the elongation of the ZnO rod, achieving a value of 1.5 min^{-1} on the ZnO-rod3−RQ $Ni_{40}Mo_{10}$ catalyst.

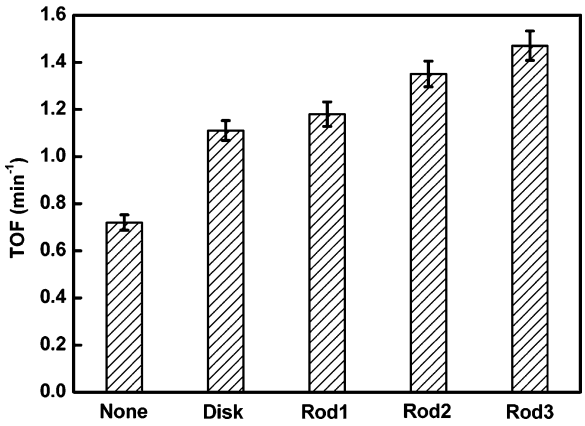

Figure 6. The production rate of 1,2-PDO over the ZnO−RQ $Ni_{40}Mo_{10}$ admixture catalysts with hexagonal ZnO crystals of different shapes. Reaction conditions: 0.5 g of RQ $Ni_{40}Mo_{10}$, ZnO/RQ $Ni_{40}Mo_{10}$ weight ratio = 1.0, T = 508 K, p_{Ar} = 3.1 MPa, and the conversion of glycerol within the range of 10−15%.

4. DISCUSSION

When employed as catalyst or cocatalyst, there are four factors that are often considered to account for the role of metal oxide: surface area,[47] crystal defect,[21,48] electronic effect,[49] and crystal habit.[50] A larger surface area usually means more surface sites on which the reactants can adsorb and react and, thus, a higher activity. For example, Deng et al. found that the ZnO hollow sphere was much more active in photodegradation of dyes than commercial ZnO, which was attributed to the larger BET surface area of the former.[47] As listed in Table 1, the total BET

dx.doi.org/10.1021/cs400526s | ACS Catal. 2013, 3, 2280−2287

surface areas of these ZnO crystals ranked as ZnO-disk > ZnO-rod2 > ZnO-rod3 > ZnO-rod1; however, according to Table 2 and Figure 6, ZnO-disk with the highest total BET surface area was the least effective in promoting the production of the hydrogenolysis products, whereas ZnO-rod1 with the lowest BET surface area performed in-between ZnO-disk and ZnO-rod2. It is evident that the total BET surface area did not dominate the promotion effect of ZnO in the CRH of glycerol.

Li et al. reported that the oxygen vacancy was more important for the catalytic activity than the BET surface area when investigating the morphology effect of ZnO in N-formylation reactions.[21] The {001} polar planes, which intrinsically possess more defects, were more active than the {100} nonpolar planes. Our Raman and PL spectra reveal that ZnO-disk is the most defective, but this sample displayed the least distinct promotion effect. On the contrary, the promotion effect of ZnO-rod3 with the highest crystal perfection was the most remarkable. These results do not favor the possibility that the promotion effect of ZnO is determined by surface defects.

A recent work showed that, when ZnO was employed as the cocatalyst with Cu nanoparticles (NPs) for methanol synthesis, the morphology of ZnO affected the selectivity to methanol by ~30%.[49] They observed by XPS, the electron transfer from platelike ZnO to Cu NPs, which was then related to the synergetic effect between physically mixed ZnO and Cu NPs. Following that work, we collected the Ni 2p and Zn 2p spectra of RQ $Ni_{40}Mo_{10}$, ZnO-rod3, and ZnO-rod3−RQ $Ni_{40}Mo_{10}$, as presented in Figure 7. For the ZnO-rod3−RQ $Ni_{40}Mo_{10}$ catalyst, the Ni $2p_{3/2}$ BE is 852.7 eV (Figure 7b), which is identical to that of bare RQ $Ni_{40}Mo_{10}$ (Figure 7a) with its Ni in the metallic state.[46] The Zn $2p_{3/2}$ BE of the ZnO-rod3−RQ $Ni_{40}Mo_{10}$ catalyst is 1021.8 eV (Figure 7d), which is the same as that of bare ZnO-rod3 (Figure 7c) with its Zn oxidation state consistent with that of bulk ZnO,[49] so the electronic interaction between ZnO and RQ $Ni_{40}Mo_{10}$ could be excluded in the ZnO−RQ $Ni_{40}Mo_{10}$ admixture catalysts.

The crystal habits have been demonstrated to exert a significant impact on the reaction due to different atomic arrangements.[51−56] Si and Flytzani-Stephanopoulos found that the CeO_2 rod enclosed by the {110} and {100} planes was more active for Au stabilization/activation than the CeO_2 cube and polyhedra in the water−gas shift reaction.[51] Co_3O_4 nanorods predominantly exposing the {110} planes not only catalyzed CO oxidation at as low as 196 K, but also remained stable in a moist stream, which was attributed to the preferential presence of Co^{3+} on these planes.[52] Among the Co_3O_4 cube, truncated octahedron, and octahedron, the octahedron with the {111} planes had the highest reversible capacity and the best rate capability as anode material in lithium ion battery.[53] The {010} planes of TiO_2 had both a favorable surface atomic structure and a surface electronic structure, which gave rise to a faster H_2 evolution rate in photocatalytic splitting of water.[54] In photodegradation of Rhodamine B on α-Fe_2O_3 with different morphologies, Zhou et al. found that α-Fe_2O_3 nanorod exposing more low-coordinated surface Fe cations was much more active than other α-Fe_2O_3.[55] Jang et al. reported that ZnO nanoplates with a high population of the Zn (0001) polar plane had the highest photocatalytic activity for H_2O_2 generation, which was understood as a result of the facile adsorption of O_2 on that plane.[56]

In our previous work,[15] we tentatively attributed the promotion effect of commercial ZnO to the CO_2-enhanced Lewis acidity of ZnO. According to Wang et al.,[16,17] CO_2 could

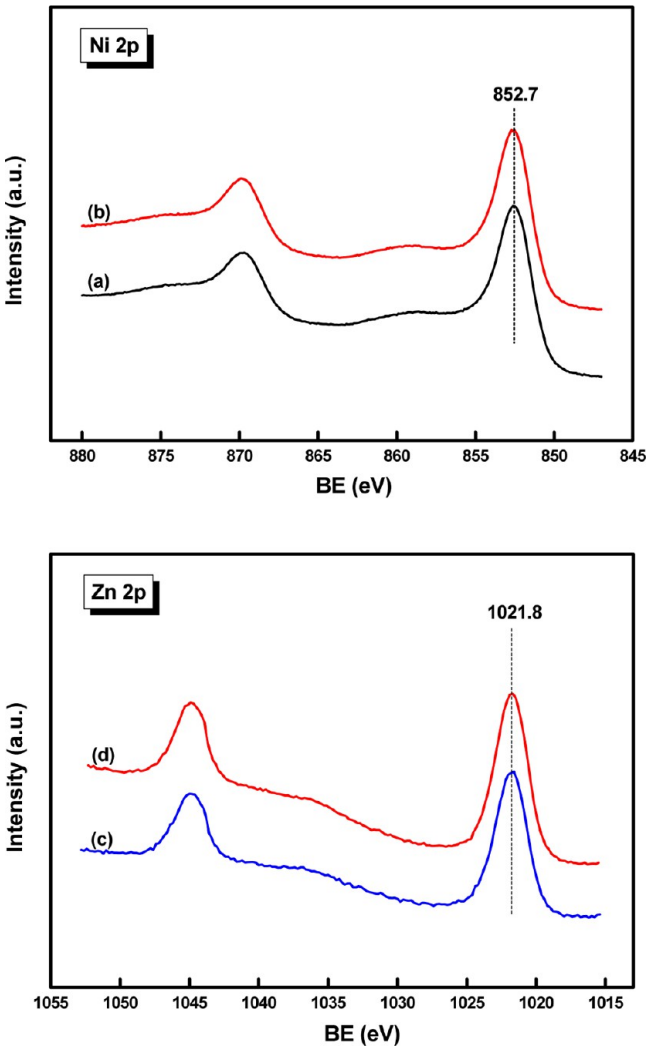

Figure 7. (Top) Ni 2p spectra of (a) bare RQ $Ni_{40}Mo_{10}$ and (b) the ZnO-rod3−RQ $Ni_{40}Mo_{10}$ admixture catalyst. (Bottom) Zn 2p spectra of (c) bare ZnO-rod3 and (d) the ZnO-rod3−RQ $Ni_{40}Mo_{10}$ admixture catalyst.

be chemisorbed and formed a stable tridentate carbonate species on the (100) nonpolar plane of ZnO, with the C atom of CO_2 bonding to one surface O anion, and both O atoms of CO_2 forming equivalent bonds with neighboring Zn cations. Note that CO_2 cannot adopt such an adsorption mode on the {001} polar planes of ZnO terminated solely with Zn^{2+} or O^{2-} ions.[20] CO_2 was adsorbed on every second Zn cation of the (100) nonpolar plane, resulting in alternating occupied and unoccupied surface Zn sites. The strong charge-accepting property of the adsorbed CO_2 made the unoccupied Zn cation more electron-deficient, which greatly enhanced the Lewis acidity of the nonpolar plane.[16] On the other hand, according to the dehydration mechanism of glycerol hydrogenolysis,[8,57,58] glycerol initially undergoes dehydration to acetol on the acid sites, which is subsequently hydrogenated to 1,2-PDO on the metallic sites. In the CRH of glycerol, CO_2 is one of the main gas products; such a CO_2-enhanced Lewis acidity of ZnO is thus expected. The addition of Lewis acidic components to accelerate the dehydration of glycerol have been widely practiced.[7,59−61] Therefore, if our argument on commercial ZnO is justified, one may anticipate a positive correlation

dx.doi.org/10.1021/cs400526s | ACS Catal. 2013, 3, 2280−2287

between the surface area of the nonpolar planes and the promotion effect of ZnO.

To validate this deduction, the relationship between the surface areas of the ZnO {100} nonpolar planes and the TOFs of 1,2-PDO was quantified. On the basis of the well-defined shape and dimension of these ZnO crystals, the BET surface areas of the {100} planes were calculated to be 1.6, 2.0, 2.9, and 3.5 $m^2\ g^{-1}$, respectively (Table 1). It is encouraging that an excellent linear relationship emerges between the BET surface area of the ZnO {100} planes and the TOF of 1,2-PDO, as plotted in Figure 8. This linearity convincingly evidences our

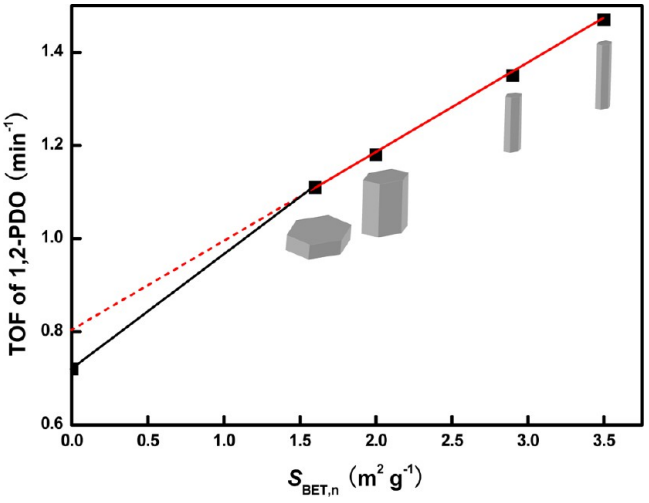

Figure 8. A plot of the TOF of 1,2-PDO over the ZnO−RQ $Ni_{40}Mo_{10}$ admixture catalysts against the S_{BET} of the {100} nonpolar planes of ZnO. Reaction conditions: 0.5 g of RQ $Ni_{40}Mo_{10}$, ZnO/RQ $Ni_{40}Mo_{10}$ weight ratio = 1.0, T = 508 K, p_{Ar} = 3.1 MPa, and the conversion of glycerol within the range of 10−15%.

hypothesis on commercial ZnO[15] and clearly verifies that the exposure degree of the {100} nonpolar planes is responsible for the shape-dependent promotion effect of ZnO in the CRH of glycerol.

Interestingly, when the straight line in Figure 8 was extended to the zero BET surface area, the extrapolated TOF of 1,2-PDO was about 11% higher than that on bare RQ $Ni_{40}Mo_{10}$, suggesting the occurrence of the synergistic effect between ZnO and RQ $Ni_{40}Mo_{10}$. It seems that the CRH of glycerol over bare RQ $Ni_{40}Mo_{10}$ is limited by its dehydration activity, rather than the hydrogenation ability. By first principles calculation of the thermodynamic profile of glycerol hydrogenolysis on transition metal catalysts including Ni, Coll et al. concluded that the metal catalyst has three roles.[44] Aside from catalyzing the hydrogenation of acetol to 1,2-PDO, it also stabilizes acetol and renders the dehydration more exothermic. Moreover, the adsorption on the surface modifies the relative stability of acetol, with implications on the reaction selectivity.

5. CONCLUSIONS

Hexagonal ZnO crystals with different aspect ratios were synthesized and employed as cocatalysts with RQ $Ni_{40}Mo_{10}$ in the CRH of glycerol. The promotion effect of these ZnO crystals was highly dependent on their crystal habits; that is, the more abundant the nonpolar planes, the more prominent the improvement in the selectivity to the hydrogenolysis products and the production rate of 1,2-PDO. The possible influences of the total surface area, crystal defects, and electronic interaction with RQ $Ni_{40}Mo_{10}$ were excluded by linking these properties with the catalytic results. The excellent linear relationship between the surface area of the {100} nonpolar planes of ZnO and the TOF of 1,2-PDO directly evidenced the assumption that the CO_2-enhanced Lewis acidity of the nonpolar planes of ZnO is responsible for the remarkable shape-dependent promotion effect of ZnO. The shape-function relationship demonstrated by this work may provide guidance for designing more effective catalyst system for the CRH of glycerol.

AUTHOR INFORMATION

Corresponding Author

*E-mail: mhqiao@fudan.edu.cn (M.H.Q.); zongbn.ripp@sinopec.com (B.N.Z.).

Notes

The authors declare no competing financial interest.

ACKNOWLEDGMENTS

This work was supported by the National Basic Research Program of China (2012CB224804), the NSF of China (21073043), the Science and Technology Commission of Shanghai Municipality (10JC1401800, 08DZ2270500), and the Program of New Century Excellent Talents (NCET-08-0126).

REFERENCES

(1) Pagliaro, M.; Ciriminna, R.; Kimura, H.; Rossi, M.; Pina, C. D. *Angew. Chem., Int. Ed.* **2007**, *46*, 4434−4440.
(2) Bienholz, A.; Schwab, F.; Claus, P. *Green Chem.* **2010**, *12*, 290−295.
(3) Brandner, A.; Lehnert, K.; Bienholz, A.; Lucas, M.; Claus, P. *Top. Catal.* **2009**, *52*, 278−287.
(4) Lahr, D. G.; Shanks, B. H. *J. Catal.* **2005**, *232*, 386−394.
(5) Maris, E. P.; Ketchie, W. C.; Murayama, M.; Davis, R. J. *J. Catal.* **2007**, *251*, 281−294.
(6) Zhou, J. X.; Guo, L. Y.; Guo, X. W.; Mao, J. B.; Zhang, S. G. *Green Chem.* **2010**, *12*, 1835−1843.
(7) Balaraju, M.; Rekha, V.; Prasad, P. S. S.; Devi, B. L. A. P.; Prasad, R. B. N.; Lingaiah, N. *Appl. Catal., A* **2009**, *354*, 82−87.
(8) Miyazawa, T.; Kusunoki, Y.; Kunimori, K.; Tomishige, K. *J. Catal.* **2006**, *240*, 213−221.
(9) Perosa, A.; Tundo, P. *Ind. Eng. Chem. Res.* **2005**, *44*, 8535−8537.
(10) Huber, G. W.; Cortright, R. D.; Dumesic, J. A. *Angew. Chem., Int. Ed.* **2004**, *43*, 1549−1551.
(11) D'Hondt, E.; Van de Vyver, S.; Sels, B. F.; Jacobs, P. A. *Chem. Commun.* **2008**, *45*, 6011−6012.
(12) Roy, D.; Subramaniam, B.; Chaudhari, R. V. *Catal. Today* **2010**, *156*, 31−37.
(13) Gandarias, I.; Arias, P. L.; Requies, J.; Güemez, M. B.; Fierro, J. L. G. *Appl. Catal., B* **2010**, *97*, 248−256.
(14) Wawrzetz, A.; Peng, B.; Hrabar, A.; Jentys, A.; Lemonidou, A. A.; Lercher, J. A. *J. Catal.* **2010**, *269*, 411−420.
(15) Hu, J. Y.; Liu, X. Y.; Fan, Y. Q.; Xie, S. H.; Pei, Y.; Qiao, M. H.; Fan, K. N.; Zhang, X. X.; Zong, B. N. *Chin. J. Catal.* **2013**, *34*, 1020−1026.
(16) Wang, Y. M.; Kováčik, R.; Meyer, B.; Kotsis, K.; Stodt, D.; Staemmler, V.; Qiu, H. S.; Traeger, F.; Langenberg, D.; Muhler, M.; Wöll, C. *Angew. Chem., Int. Ed.* **2007**, *46*, 5624−5627.
(17) Wang, Y. M.; Xia, X.; Urban, A.; Qiu, H. S.; Strunk, J.; Meyer, B.; Muhler, M.; Wöll, C. *Angew. Chem., Int. Ed.* **2007**, *46*, 7315−7318.
(18) Somorjai, G. A. *Introduction to Surface Chemistry and Catalysis*; John Wiley & Sons: New York, 1994, Chapter 7.
(19) Garcia, S. P.; Semancik, S. *Chem. Mater.* **2007**, *19*, 4016−4022.
(20) Wang, Z. L. *J. Phys.: Condens. Matter* **2004**, *16*, R829−R858.
(21) Li, G. R.; Hu, T.; Pan, G. L.; Yan, T. Y.; Gao, X. P.; Zhu, H. Y. *J. Phys. Chem. C* **2008**, *112*, 11859−11864.

(22) Peng, Y.; Xu, A. W.; Deng, B.; Antonietti, M.; Cölfen, H. *J. Phys. Chem. B* **2006**, *110*, 2988−2993.
(23) Cheng, B.; Samulski, E. T. *Chem. Commun.* **2004**, *8*, 986−987.
(24) Vayssieres, L. *Adv. Mater.* **2003**, *15*, 464−466.
(25) Hu, J. Q.; Li, Q.; Wong, N. B.; Lee, C. S.; Lee, S. T. *Chem. Mater.* **2002**, *14*, 1216−1219.
(26) Shen, L.; Bao, N.; Yanagisawa, K.; Domen, K.; Grimes, C. A.; Gupta, A. *J. Phys. Chem. C* **2007**, *111*, 7280−7287.
(27) Yoshida, Y.; Mitani, Y.; Itoi, T.; Izumi, Y. *J. Catal.* **2012**, *287*, 190−202.
(28) Bai, S.; Hu, J. W.; Li, D.; Luo, R.; Chen, A.; Liu, C. C. *J. Mater. Chem.* **2011**, *21*, 12288−12294.
(29) Guo, L.; Ji, Y. L.; Xu, H. B. *J. Am. Chem. Soc.* **2002**, *124*, 14864−14865.
(30) Wang, G.; Deng, Y.; Guo, L. *Chem.—Eur. J.* **2010**, *16*, 10220−10225.
(31) Xu, F.; Zhang, P.; Navrotsky, A.; Yuan, Z. Y.; Ren, T. Z.; Halasa, M.; Su, B. L. *Chem. Mater.* **2007**, *19*, 5680−5686.
(32) Kuo, C. L.; Kuo, T. J.; Huang, M. H. *J. Phys. Chem. B* **2005**, *109*, 20115−20121.
(33) Tong, Y.; Liu, Y.; Dong, L.; Zhao, D.; Zhang, J.; Lu, Y.; Shen, D.; Fan, X. *J. Phys. Chem. B* **2006**, *110*, 20263−20267.
(34) Li, P.; Liu, H.; Lu, B.; Wei, Y. *J. Phys. Chem. C* **2010**, *114*, 21132−21137.
(35) Umar, A.; Hahn, Y. B. *Appl. Phys. Lett.* **2006**, *88*, 173120−173122.
(36) Wu, J. J.; Liu, S. C. *J. Phys. Chem. B* **2002**, *106*, 9546−9551.
(37) Cong, G. W.; Wei, H. Y.; Zhang, P. F.; Peng, W. Q.; Wu, J. J.; Liu, X. L.; Jiao, C. M.; Hu, W. G.; Zhu, Q. S.; Wang, Z. G. *Appl. Phys. Lett.* **2005**, *87*, 231903−231906.
(38) Wu, J. J.; Liu, S. C. *Adv. Mater.* **2002**, *14*, 215−218.
(39) Beane, G. A.; Morfa, A. J.; Funston, A. M.; Mulvaney, P. *J. Phys. Chem. C* **2012**, *116*, 3305−3310.
(40) Wu, X. L.; Siu, G. G.; Fu, C. L.; Ong, H. C. *Appl. Phys. Lett.* **2001**, *78*, 2285−2287.
(41) Andelman, T.; Gong, Y. Y.; Polking, M.; Yin, M.; Kuskovsky, I.; Neumark, G.; O'Brien, S. *J. Phys. Chem. B* **2005**, *109*, 14314−14318.
(42) Strunk, J.; Kahler, K.; Xia, X.; Muhler, M. *Surf. Sci.* **2009**, *603*, 1776−1783.
(43) Auneau, F.; Michel, C.; Delbecq, F.; Pinel, C.; Sautet, P. *Chem.—Eur. J.* **2011**, *17*, 14288−14299.
(44) Coll, D.; Delbecq, F.; Aray, Y.; Sautet, P. *Phys. Chem. Chem. Phys.* **2011**, *13*, 1448−1456.
(45) Cortright, R. D.; Davda, R. R.; Dumesic, J. A. *Nature* **2002**, *418*, 964−967.
(46) Xie, F. Z.; Chu, X. W.; Hu, H. R.; Qiao, M. H.; Yan, S. R.; Zhu, Y. L.; He, H. Y.; Fan, K. N.; Li, H. X.; Zong, B. N.; Zhang, X. X. *J. Catal.* **2006**, *241*, 211−220.
(47) Deng, Z.; Chen, M.; Gu, G.; Wu, L. *J. Phys. Chem. B* **2008**, *112*, 16−22.
(48) Xu, L.; Hu, Y. L.; Pelligra, C.; Chen, C. H.; Jin, L.; Huang, H.; Sithambaram, S.; Aindow, M.; Joesten, R.; Suib, S. L. *Chem. Mater.* **2009**, *21*, 2875−2885.
(49) Liao, F.; Huang, Y.; Ge, J.; Zheng, W.; Tedsree, K.; Collier, P.; Hong, X.; Tsang, S. C. *Angew. Chem., Int. Ed.* **2011**, *50*, 2162−2165.
(50) Xia, S.; Yuan, Z.; Wang, L.; Chen, P.; Hou, Z. *Appl. Catal., A* **2011**, *403*, 173−182.
(51) Si, R.; Flytzani-Stephanopoulos, M. *Angew. Chem., Int. Ed.* **2008**, *47*, 2884−2887.
(52) Xie, X. W.; Li, Y.; Liu, Z. Q.; Haruta, M.; Shen, W. J. *Nature* **2009**, *458*, 746−749.
(53) Xiao, X. L.; Liu, X. F.; Zhao, H.; Chen, D. F.; Liu, F. Z.; Xiang, J. H.; Hu, Z. B.; Li, Y. D. *Adv. Mater.* **2012**, *24*, 5762−5766.
(54) Pan, J.; Liu, G.; Lu, G. Q.; Cheng, H. M. *Angew. Chem., Int. Ed.* **2011**, *50*, 2133−2137.
(55) Zhou, X.; Lan, J.; Liu, G.; Deng, K.; Yang, Y.; Nie, G.; Yu, J.; Zhi, L. *Angew. Chem., Int. Ed.* **2012**, *51*, 178−182.
(56) Jang, E. S.; Won, J. H.; Hwang, S. J.; Choy, J. H. *Adv. Mater.* **2006**, *18*, 3309−3312.
(57) Miyazawa, T.; Koso, S.; Kunimori, K.; Tomishige, K. *Appl. Catal., A* **2007**, *318*, 244−251.
(58) Miyazawa, T.; Koso, S.; Kunimori, K.; Tomishige, K. *Appl. Catal., A* **2007**, *329*, 30−35.
(59) Chai, S. H.; Wang, H. P.; Liang, Y.; Xu, B. Q. *Green Chem.* **2007**, *9*, 1130−1136.
(60) Alhanash, A.; Kozhevnikova, E. F.; Kozhevnikov, I. V. *Appl. Catal., A* **2010**, *378*, 11−18.
(61) Katryniok, B.; Paul, S.; Bellière-Baca, V.; Reye, P.; Dumeignil, F. *Green Chem.* **2010**, *12*, 2079−2098.